PCCP

PAPER

View Article Online
View Journal | View Issue

Check for updates

Cite this: Phys. Chem. Chem. Phys., 2024, 26, 5289

Revisiting ultrasmall phosphine-stabilized rhodium-doped gold clusters Au_nRh (n = 5, 6, 7, 8): geometric, electronic, and vibrational properties†

Jenica Marie L. Madridejos, [ab] Jason F. Alvino, [a] Yunpeng Lu, [b]
Vladimir B. Golovko [c] and Gregory F. Metha *[a]

Received 8th December 2023,
Accepted 7th January 2024

DOI: 10.1039/d3cp05976f

rsc.li/pccp

Incorporation of other transition metals in Au nanoclusters has been thriving recently due to its effect on their electronic and photophysical properties. Here, the ultrasmall phosphine-stabilized Rh-doped gold clusters Au_nRh (n = 5, 6, 7, 8), with metal core structures represented as fragments of a rhodium-centered icosahedron, are considered. The geometric and electronic properties of these nanoclusters are revisited and analyzed using density functional theory (DFT). Moreover, infrared spectra are simulated to identify the effects of Rh doping on the clusters through vibrational properties. Peaks are assigned to breathing-like normal modes for all AuRh clusters except for Au_8Rh, likely due to the presence of bound Cl ligands. Unlike their pure gold core counterparts, the % motions of both Au and Rh atoms are lower in the mixed metal clusters, suggesting more restrained metal cores by rhodium, which could result in other novel physical and chemical properties not hitherto discovered.

1 Introduction

Ligand-stabilized atomically-precise metal nanoclusters have generated tremendous interest over the recent years because of their distinct physicochemical properties and potential applications.[1] A large number of structurally determined nanoclusters with defined elemental compositions have been prepared in the past decade, with various ligands used for stabilization. In ultrasmall gold nanoparticles, there has been an increasing interest in the understanding of transition bimetallic clusters. Doping a different transition metal atom into a metal cluster dramatically changes the electronic properties and catalytic behaviour of the host cluster.[2–5] There have been extensive theoretical and experimental studies on noble metal clusters such as Au and Ag, most especially due to their distinctive chemical properties. In early work on gas phase cationic $Au_nX_m^+$ clusters (X = Cu, Al, Y, and In), the cluster geometries and electronic shell were shown to depend on the nature of dopant atoms.[6] Heinebrodt *et al.* described the binding patterns of Au with Al, In, and Cs, wherein charge transfer takes place between Au and In while ionic interaction prevails between Au and Cs.[7] Additionally, anionic binary Au_nM^- clusters (M = Pd, Ni, Zn, Cu, and Mg) were explored by Koyasu *et al.* using anion photoelectron spectroscopy.[8] Density functional theory (DFT) studies of neutral bimetallic gold clusters have also been reported for Ni, Pd and Pt,[9] Fe,[10] Ag and Cu,[11] Ti,[12] Sc,[13] and Rh.[14] Buendia *et al.* reported the experimental and theoretical photoelectron (PES) and IR spectra of neutral and anionic non-ligated Au_nRh_m (n = 1–7 and m = 1–2) clusters in vacuum.[15] Additionally, mechanistic insight into the catalyzed hydrogenation reaction revealed that the activation barrier of monorhodium-doped gold clusters is reduced compared to pure gold clusters.[3] Notably, transition metal-doped gold clusters have been comprehensively studied due to their synergistic effects on catalysis.[1,16] Tsukuda and co-workers reported the use of Pd- and Rh-doped Au_{34} superatom for hydrogenation catalysis wherein Rh-doped Au:PVP cluster proved to be superior.[4,5] Recently, doping metals onto Au_{13} nanoclusters has been observed to enhance quantum yield with an increased HOMO–LUMO gap and was reported to act as more efficient and stable photocatalysts.[17]

Decades ago, Bott *et al.* reported a series of ultrasmall gold-rhodium clusters Au_nRh clusters (n = 5–8) with triphenylphosphine groups as their main ligands: $[Au_5Rh(PPh_3)_5(C_9H_9N)_3]^{2+}$, $[Au_6Rh(PPh_3)_6(CO)_2]^+$, $[Au_7Rh(PPh_3)_7(CO)_2]^{2+}$, and $[Au_8Cl_2(PPh_3)_6$-

---

[a] Department of Chemistry, The University of Adelaide, South Australia 5005, Australia. E-mail: greg.metha@adelaide.edu.au
[b] School of Chemistry, Chemical Engineering and Biotechnology, Nanyang Technological University, Singapore 639798, Singapore
[c] The MacDiarmid Institute for Advanced Materials and Nanotechnology, Department of Chemistry, University of Canterbury, Christchurch, 8140, New Zealand

† Electronic supplementary information (ESI) available. See DOI: https://doi.org/10.1039/d3cp05976f

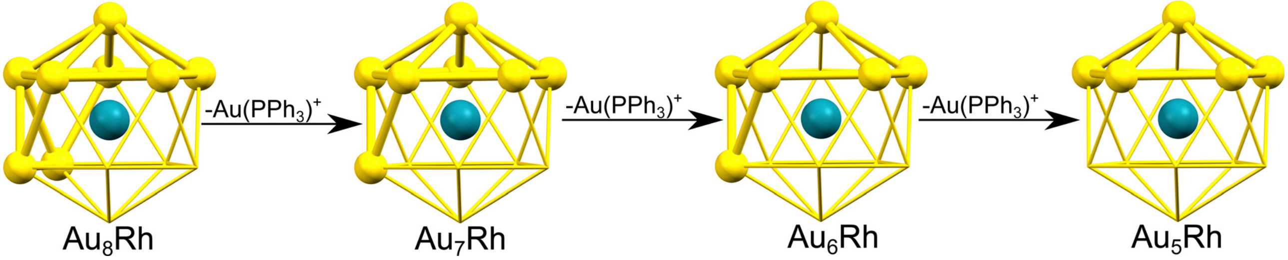

Fig. 1 The structural relationship among the AuRh clusters synthesized by Bott *et al.*[18] The idealized metal core geometries are shown as fragments of a centered icosahedron with rhodium atom (turquoise) at the center.

$Rh(C_9H_9N)_2]^+$ (hereafter referred to as Au_5Rh, Au_6Rh, Au_7Rh, and Au_8Rh, respectively).[18] Their gold-rhodium cores were all found to be structurally represented as fragments of the rhodium-centered icosahedron in Fig. 1. Based on the structures of the Au_nRh core alone, the lower-numbered gold-rhodium clusters could be obtained from the sequential removal of $Au(PPh_3)$ moieties of the Au_8Rh cluster. In this study, we analyze the geometric and electronic structures of this series of Au_nRh clusters using density functional theory based on their experimental crystal structures.

Takano *et al.* have reported the importance of core rigidification by the ligands in the effective photoluminescence of Ru-doped Au_{12} clusters.[19] Metal core motion and ligand suppression can be analyzed using infrared spectroscopy by detecting the vibrational modes of key functional groups. Several studies have reported the IR spectra of ligand-stabilized gold clusters,[20–23] but we are not aware of any involving the Au_nRh clusters. This present work extends our previous far-IR and computational studies of atomically precise gold-based clusters[20,21] and ruthenium-based clusters[24] to ligand-protected bimetallic Au_nRh clusters (n = 5–8) focused on low frequency vibrational modes (λ = 50–450 cm^{-1}).

2 Computational details

Geometry optimization and harmonic vibrational frequency calculations (including force constant, k) of the fully-ligated Au_5Rh, Au_6Rh Au_7Rh, and Au_8Rh clusters were performed using M06 density functional[25] with all atoms treated with the LANL2DZ basis set and related effective core potentials (ECP)[26] using the Gaussian 09 suite of programs.[27] This level of theory has been used for similar metal cluster systems previously, and has shown good agreement to experimental far IR spectra.[20,24] Initial geometries of Au_5Rh (CSD Refcode KOFTOO), Au_7Rh (CSD Refcode KOFVAC), Au_8Rh (CSD Refcode JAPWOM) were taken from previously reported X-ray crystal structures of the synthesized clusters deposited in the Cambridge Crystallographic Database.[28] The initial structure of Au_6Rh was based on the description of Bott *et al.* wherein one $AuPPh_3$ unit in an equatorial position of Au_7Rh is removed.[18] Counter ions were removed, with the appropriate number of electrons removed from the calculations to balance the charge and no symmetry constraints were used in the calculations. After optimization, a frequency calculation was performed to confirm that the optimized geometry is a true minimum without any imaginary frequencies. To obtain the simulated IR spectra, all peaks were convoluted with a Gaussian line shape function with 8 cm^{-1} full width at half-maximum (FWHM). The Cartesian coordinates of the optimized structures for these four clusters are also provided in the ESI.†

3 Results and discussion

3.1 Geometric parameters and ligand binding energies

The optimized structures of the Au_nRh clusters are shown in Fig. 2. Both Au_6Rh and Au_7Rh have 2 carbonyl ligands attached to the Rh atom while Au_5Rh and Au_8Rh have 3 and 2 isocyanide-based xylyl ligands attached on their central Rh atom, respectively. The Au_8Rh also has additional Cl atoms attached to two Au atoms. For all Au_nRh clusters in this study, the ligands attached to the Rh atom are known to be easily removed. Moreover, the PPh_3 ligands attached on the Au atoms

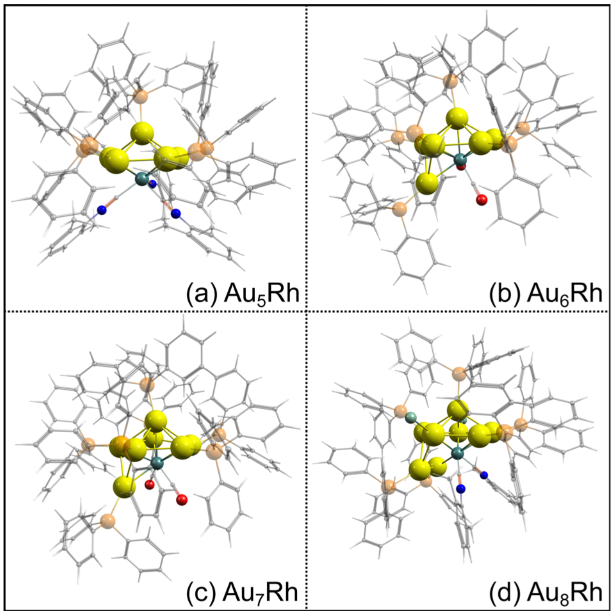

Fig. 2 Optimized structures of the fully ligated (a) Au_5Rh, (b) Au_6Rh, (c) Au_7Rh, and (d) Au_8Rh clusters. Au, Rh, N, O, and P atoms are represented by yellow, turquoise, blue, red, and orange spheres, respectively. C and H atoms are represented by transparent gray and white spheres, respectively.

also require lower temperature to be removed than their thiolate counterparts.[29] The DFT-optimized structures have longer bond lengths when compared to the crystal structures because the experimental geometries are tightly-packed in condensed phase rather than in "gas-phase" of the calculations. Even so, a close match between the optimized geometries and experimental crystal structures is observed for the gold-rhodium clusters (Fig. S1, ESI†).

To calculate the binding energies of the ligands in Table 1, we use the following equation:

$$BE_{\text{ave}} = \frac{E_{\text{total}} - \left(N \times E_{\text{ligand}} + E_{\text{complex}}\right)}{N} \tag{1}$$

where E_{total} is the total energy of the fully ligated clusters, N is the number of ligands under consideration, E_{ligand} is the energy of free PPh_3, xylyl, or CO ligand under consideration and E_{complex} is the rest of the cluster without the ligand(s) under study. For example, the average binding energy of the xylyl ligands on Au_5Rh is calculated with $N = 2$ and E_{complex} as the energy of $[Au_5(PPh_3)_5]^{2+}$, whereas the average binding energy of PPh_3 on Au_5Rh is calculated with $N = 5$ and E_{complex} as the energy of $[Au_5(C_9H_9N)_3]^{2+}$. The calculated average binding energies of PPh_3 in all gold-rhodium clusters are 44–59 kcal mol^{-1}, consistent with previous studies.[29–33] These values are consistent with a temperature range of 150–200 °C required to fully remove the triphenylphosphine ligands.[34,35] Both xylyl and C=O ligands of Rh atom have similar average binding energies to PPh_3.

3.2 Electronic structure

The Au_nRh clusters offer a specific perspective into the contribution of Rh to the electronic structure. Tsukuda and co-workers summarized the effect of doping on the spherical superatoms of gold clusters using the jellium model.[36] When dopants are more electronegative (such as Pt, Pd, and Rh) than gold, the superatomic orbitals are destabilized due to reductions of the effective positive charge of the core, resulting in an upshift to their energy levels. This is only observed when icosahedral Au cores are considered. However, the Au_nRh clusters presented here are fragments of a centered icosahedron, Au_{13}, as shown in Fig. 1. Therefore, we can also consider z-axis compression based on the closed-shell electron count of Hakkinen's superatom concept (SAC) equation.[37] If Rh is considered as another Au atom, we expect the following electron count for the Au_nRh clusters: 4e (Au_5Rh) and 6e (Au_6Rh, Au_7Rh, Au_8Rh). Thus, the Au_5Rh cluster is expected to adopt a prolate shape with z-axis expansion while the others have an oblate shape with z-axis compression. This in turn results in an orbital with $1p_z$ character for the Au_5Rh HOMO and $1p_x$ and $1p_y$ character for the LUMO and LUMO+1, respectively. On the other hand, 6e clusters should exhibit $1p_x$ and $1p_y$ characteristics for HOMO and HOMO–1, and $1p_z$ and 1d character for the LUMO and LUMO+1 orbitals.

The topological plots of the frontier molecular orbitals (FMO) of the Au_nRh clusters are shown in Fig. 3. All FMO plots reveal that the HOMO−1, HOMO, LUMO, and LUMO+1 are mainly localized on the AuRh core (Tables S1 and S2, ESI†). The contribution of Rh in the HOMO of Au_5Rh is significantly higher than the other clusters, with approximately 1 : 1 ratio of Au and Rh contributions to the orbital based on the results of three different partition methods. Interestingly, the shapes of the frontier MOs of Au_5Rh deviate from the expected trend based on SAC electron count and z-axis expansion discussed above. The HOMO−1, HOMO, and LUMO all have 1p characteristics while the LUMO+1 displays 1d character in Au_5Rh, similar to Au_6Rh and Au_7Rh. This suggests an effect from the heteroatom on the electronic properties of the Au_5Rh cluster, wherein the Rh contribution on the HOMO is evident by the presence of its δ orbitals. The Au_8Rh cluster has similar FMO characteristics as the butterfly structure of $[Au_9(PPh_3)_8]^{3+}$,[38] wherein the LUMO has 1d character while the LUMO+1 has 1p character, evidently similar to the previous MO calculations presented by Mingos and co-workers.[39] Both the structures of Au_8Rh and the butterfly isomer of Au_9 are toroidal rather than spherical in shape such as in the case of the crown isomer of Au_9 and Au_8Pd.[38–40] This difference in the bonding pattern causes the $1p_z$ orbital to be higher in energy, making it unavailable for skeletal bonding and subsequently deviating from the expected MO trend based on electron count. Additionally, the contribution of δ orbitals from Rh stabilizes the LUMO+1 ($1p_z$) orbital of Au_8Rh. The trend of the HOMO–LUMO energy gaps of the AuRh clusters is also consistent with the colors of the synthesized crystals. The Au_7Rh and Au_8Rh clusters both have a relatively low calculated energy gap of ∼3.20 eV and both exhibit a red color. On the other hand, Au_6Rh has an orange-like color while Au_5Rh has a distinct yellow color, and with both having larger HOMO–LUMO energy gaps calculated to be 3.42 and 3.82 eV, respectively.

3.3 Far IR spectroscopy

The DFT-simulated far IR spectra of the four Au_nRh clusters are presented in Fig. 4. A summary of the peak assignments for each cluster is shown in Tables S3 to S6, ESI.† The normal coordinate motions that involve significant motion of Au, Rh, P, and Cl (for Au_8Rh) are identified and shown as percentages of total non-mass-weighted atomic motion. The simulated spectra were scaled from the DFT-calculated numbers by a functional-independent correction factor (eqn (2)) used previously for low-frequency vibrations.[41]

$$\tilde{\nu}_{\text{corr}} = 22\ \text{cm}^{-1} + \tilde{\nu}_{\text{calc}} \times 0.94 \tag{2}$$

Generally, all four clusters exhibit large peaks between 430–450 cm^{-1} which were previously assigned to distortion of the

Table 1 Summary of the average binding energies in kcal mol^{-1} of the ligands on Au_5Rh, Au_6Rh, Au_7Rh, and Au_8Rh clusters based on eqn (1) using M06/LANL2DZ level of theory

Cluster	BE_{ave} of Rh-bound ligands	BE_{ave} of PPh_3
Au_5Rh	51.2 (xylyl)	56.9
Au_6Rh	51.3 (CO)	43.6
Au_7Rh	49.7 (CO)	59.1
Au_8Rh	56.8 (xylyl)	48.5

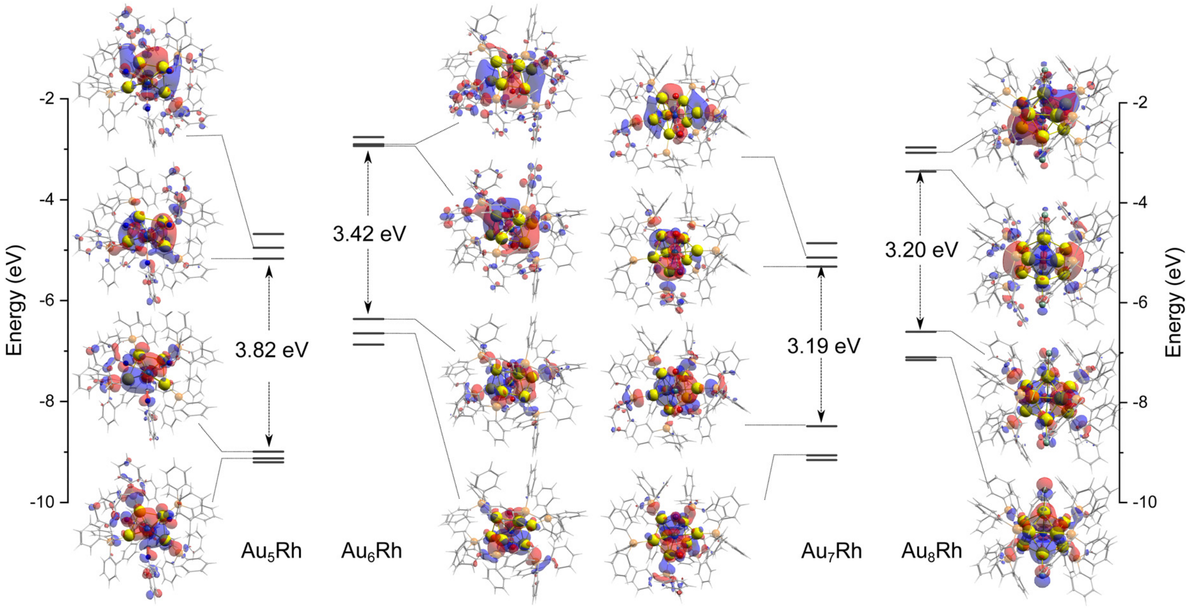

Fig. 3 The plots of frontier molecular orbital (HOMO−1, HOMO, LUMO, LUMO+1) of Au_5Rh, Au_6Rh, Au_7Rh, and Au_8Rh clusters as calculated by M06/LANL2DZ with an isosurface value of 0.02 a.u.

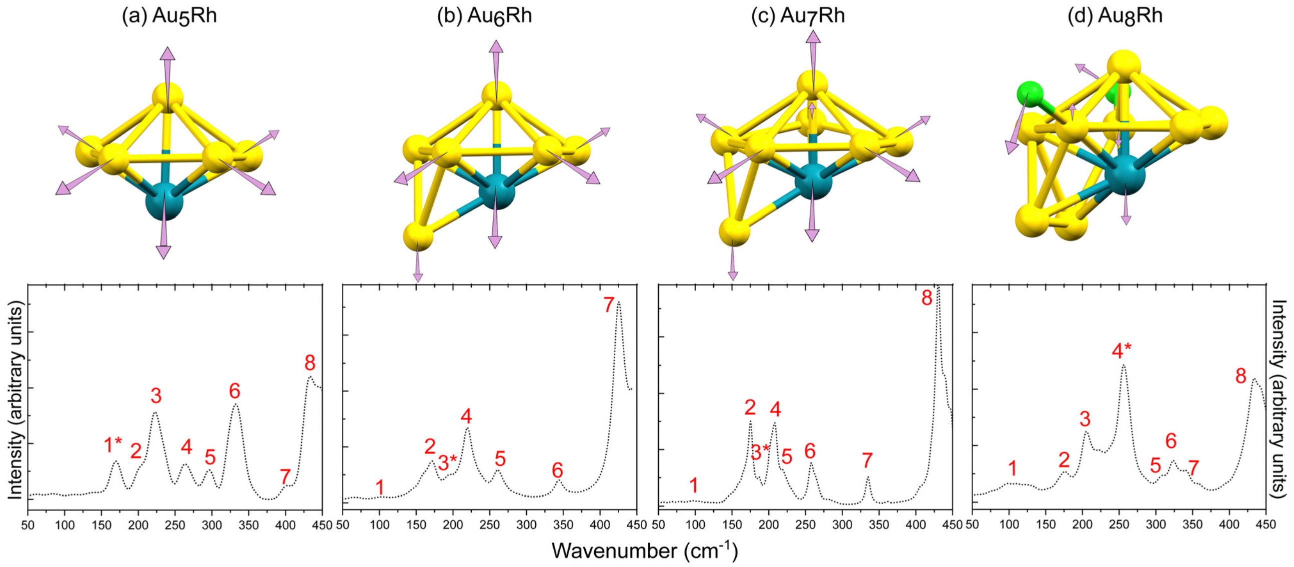

Fig. 4 Calculated normal mode displacements associated with the cluster core vibrations for (a) Au_5Rh at 164.3 cm^{-1}, (b) Au_6Rh at 182.5 cm^{-1}, (c) Au_7Rh at 175.4 cm^{-1}, and (d) Au_8Rh at 246.7 cm^{-1}. The simulated (bottom) far-IR spectra of the Au_nRh clusters are also shown and numbered based on their peak assignments in the ESI.† The IR peaks denoted with asterisks are those assigned to the calculated normal mode displacements presented.

triphenylphosphine ligands (PPh_3), while peaks $<250\ cm^{-1}$ are transitions involving the Au core distortions.[20,24]

3.3.1 Au_5Rh cluster. The first broad peak is assigned to AuRh core distortions, one of which is the breathing mode shown in Fig. 4a. The breathing modes are a distinguishing feature for large metal nanoparticles and their linear dependence on the nanoparticle diameter has been investigated using time-resolved pump–probe spectroscopy and continuum mechanics.[42] Low-frequency symmetric breathing modes have been experimentally detected as Raman active in several ligand-stabilized atomically-precise Au nanoclusters[23,43] and the nature of bonding with the ligands affect the confinement of these gold vibrational modes.[44]

The % Au motions of Au_5Rh are significantly lower than previously found for Au_6; 14–16% Au motion in the previous study[20] but only 1.2% Au and 0.3% Rh motion in Au_5Rh. The vibrations arising from the xylyl ligands appear from 220 cm^{-1} onwards and the Rh–C wagging and twisting motions are assigned to the large peaks at 300 and 330 cm^{-1}, respectively. The normal modes of vibration due to PPh$_3$ ligands are visible at 260 and 430 cm^{-1} as has been previously reported.[20]

3.3.2 Au$_6$Rh cluster. The description of the Au$_6$Rh core by Bott *et al.* allowed the simulation of the IR spectrum even without an experimental crystal structure. The DFT-optimized structure is shown in the ESI.† The first peak is assigned to metal core distortion, primarily from Au atoms, while the 2nd and 4th peaks account for Au–Rh–Au symmetric and asymmetric stretching, respectively. The breathing mode of the metal core (Fig. 4b) is assigned to the peak at 195 cm^{-1}. We can compare the % metal motions of this cluster with Au$_6$Pd from our previous study.[20] Interestingly, the % Au and % Rh motion for Au$_6$Rh are lower than its Pd-doped counterpart that has significant % Pd contributions ranging from 1–5%. The largest total metal motion (5.87%) for Au$_6$Rh is assigned to the Au–Rh–Au asymmetric stretching. The % Au motion of Au$_6$Rh is only 3.3% whereas it reaches ∼8% Au motion for the Au$_6$Pd cluster. Based on these observations, Rh-doping seems to stiffen the Au core more than the Pd-doping. Finally, the pronounced single peak at 340 cm^{-1} is assigned to Rh–C–O rocking and the large peak at 425 cm^{-1} comes from PPh$_3$ distortions.

3.3.3 Au$_7$Rh cluster. The small broad peak at 100 cm^{-1} is assigned to a low-intensity Au core distortion. Next, there are three prominent peaks between 170–260 cm^{-1}. The peak at 175 cm^{-1} is assigned to Au core distortion, with 3.46% Au motion (in Table S5, ESI†), which is also remarkably lower than previously reported for Au$_8$ that ranges from 16–20%.[20] There is a tiny shoulder at 185 cm^{-1} which is assigned to the breathing mode of the Au$_7$Rh core (Fig. 4c). The peak at 210 cm^{-1} is a convolution of different transitions displaying Au–Au stretches and the next peak at 260 cm^{-1} is assigned to PPh$_3$ distortions. The wagging of the carbonyl group is assigned to the small peak at 335 cm^{-1}, similar to Au$_6$Rh, while the large peaks at 400–450 cm^{-1} are assigned to PPh$_3$ distortions. Both Au$_6$Rh and Au$_7$Rh reveal stronger contributions from the heavy metals than Au$_5$Rh and Au$_8$Rh (*vide infra*) for the Au core distortion and AuRh breathing modes. This can be attributed to the lighter CO ligands attached to the Rh central atom that permit more motion of the heavy metals than the heavier xylyl ligands present in both Au$_5$Rh and Au$_8$Rh.

3.3.4 Au$_8$Rh cluster. No breathing mode is observed for the Au$_8$Rh core unlike the smaller AuRh clusters. This can be explained by the presence of heavy Cl ligands on two Au atoms which also reduces the symmetry of the cluster. Furthermore, the % Rh motions are noticeably lower for the IR peaks that are assigned to the metal core transitions between 70–230 cm^{-1} while a Cl wagging motion with 2.26% motion is observed in the same region, as summarized in Table S6 (ESI†). The highest % metal core motion of Au$_8$Rh is 2.77% which is much lower than 8–17% for Au core distortion of Au$_9$.[20] The primary peak at 247 cm^{-1} is assigned to the asymmetric Au–Cl stretch with only 1.61% Au but 7.66% Cl motion. In the case of Au$_8$Rh cluster, it is observed that not only the presence of Rh but also Cl inhibits the motion of the Au core. Peaks 5–7 are assigned to vibrations of the xylyl ligands attached to the Rh atom, similar to peaks 5 and 6 of the Au$_5$Rh cluster.

4 Conclusion

We report the geometric, electronic, and vibrational properties of ultrasmall bimetallic gold-rhodium nanoclusters Au$_n$Rh (n = 5, 6, 7, and 8). The average ligand binding energies are calculated to be ∼50 kcal mol^{-1}, which is low enough to be removed at calcination temperatures of 150–200 °C. The calculated electronic properties indicate a stabilization effect of the Rh atom in the Au$_5$Rh and Au$_8$Rh clusters. Additionally, the calculated HOMO–LUMO energy gap trend corresponds to the observed colors of the respective crystals. The metal core transitions are significantly affected by the presence of the Rh atom which inhibits the motion of Au atoms as observed in the simulated IR spectra. Likewise, all clusters display the symmetric breathing mode of the AuRh core except for Au$_8$Rh due to the presence of Cl ligands.

Conflicts of interest

There are no conflicts to declare.

Acknowledgements

J. M. L. M. acknowledges previous financial support from Adelaide Scholarship International (ASI), Future Fuels Cooperative Research Center (FFCRC), and the Ministry of Education, Singapore, under its Academic Research Fund Tier 1 RG83/20. Supercomputing resources at the University of Adelaide and Nanyang Technological University were provided by the Phoenix and Gekko HPC services, respectively.

Notes and references

1 (*a*) H. Qian, M. Zhu, Z. Wu and R. Jin, *Acc. Chem. Res.*, 2012, **45**, 1470–1479; (*b*) G. Li and R. Jin, *Acc. Chem. Res.*, 2013, **46**, 1749–1758; (*c*) S. Yamazoe, K. Koyasu and T. Tsukuda, *Acc. Chem. Res.*, 2014, **47**, 816–824; (*d*) R. Jin, C. Zeng, M. Zhou and Y. Chen, *Chem. Rev.*, 2016, **116**, 10346–10413; (*e*) I. Chakraborty and T. Pradeep, *Chem. Rev.*, 2017, **117**, 8208–8271; (*f*) Z. Lei, X.-K. Wan, S.-F. Yuan, Z.-J. Guan and Q.-M. Wang, *Acc. Chem. Res.*, 2018, **51**, 2465–2474; (*g*) R. R. Nasaruddin, T. Chen, N. Yan and J. Xie, *Coord. Chem. Rev.*, 2018, **368**, 60–79; (*h*) Y. Du, H. Sheng, D. Astruc and M. Zhu, *Chem. Rev.*, 2020, **120**, 526–622; (*i*) R. H. Adnan, J. M. L. Madridejos, A. S. Alotabi, G. F. Metha and G. G. Andersson, *Adv. Sci.*, 2022, **9**, 2105692.

2 (*a*) R. Jin and K. Nobusada, *Nano Res.*, 2014, **7**, 285–300; (*b*) Y. Negishi, W. Kurashige, Y. Niihori, T. Iwasa and K. Nobusada, *Phys. Chem. Chem. Phys.*, 2010, **12**, 6219; (*c*) S. Wang, Y. Song, S. Jin, X. Liu, J. Zhang, Y. Pei, X. Meng, M. Chen, P. Li and M. Zhu, *J. Am. Chem. Soc.*, 2015, **137**, 4018–4021; (*d*) L. Liao, S. Zhou, Y. Dai, L. Liu,

C. Yao, C. Fu, J. Yang and Z. Wu, *J. Am. Chem. Soc.*, 2015, **137**, 9511–9514; (*e*) M. Zhou, H. Qian, M. Y. Sfeir, K. Nobusada and R. Jin, *Nanoscale*, 2016, **8**, 7163–7171; (*f*) S. Takano, H. Hirai, S. Muramatsu and T. Tsukuda, *J. Am. Chem. Soc.*, 2018, **140**, 8380–8383.

3 T. Sengupta, J. S. Chung and S. G. Kang, *Nanoscale*, 2020, **12**, 5125–5138.

4 S. Hayashi, R. Ishida, S. Hasegawa, S. Yamazoe and T. Tsukuda, *Top. Catal.*, 2018, **61**, 136–141.

5 S. Hasegawa, S. Takano, S. Yamazoe and T. Tsukuda, *Chem. Commun.*, 2018, **54**, 5915–5918.

6 W. Bouwen, F. Vanhoutte, F. Despa, S. Bouckaert, S. Neukermans, L. Theil Kuhn, H. Weidele, P. Lievens and R. E. Silverans, *Chem. Phys. Lett.*, 1999, **314**, 227–233.

7 M. Heinebrodt, N. Malinowski, F. Tast, W. Branz, I. M. L. Billas and T. P. Martin, *J. Chem. Phys.*, 1999, **110**, 9915–9921.

8 K. Koyasu, Y. Naono, M. Akutsu, M. Mitsui and A. Nakajima, *Chem. Phys. Lett.*, 2006, **422**, 62–66.

9 D. W. Yuan, Y. Wang and Z. Zeng, *J. Chem. Phys.*, 2005, **122**, 114310.

10 D. Die, X.-Y. Kuang, J.-J. Guo and B.-X. Zheng, *J. Mol. Struct. THEOCHEM*, 2009, **902**, 54–58.

11 Y. Xu, C. Xu, T. Zhou and C. Cheng, *J. Mol. Struct. THEOCHEM*, 2009, **893**, 88–92.

12 M.-X. Chen and X. H. Yan, *J. Chem. Phys.*, 2008, **128**, 174305.

13 G.-x. Ge, H.-x. Yan and Q. Jing, *Chin. J. Chem. Phys*, 2010, **23**, 416–424.

14 J.-X. Yang, C.-F. Wei and J.-J. Guo, *Phys. B Condens. Matter*, 2010, **405**, 4892–4896.

15 F. Buendía, M. R. Beltrán, X. Zhang, G. Liu, A. Buytendyk and K. Bowen, *Phys. Chem. Chem. Phys.*, 2015, **17**, 28219–28227.

16 (*a*) N. Toshima and T. Yonezawa, *New J. Chem.*, 1998, **22**, 1179–1201; (*b*) T. Balcha, J. R. Strobl, C. Fowler, P. Dash and R. W. J. Scott, *ACS Catal.*, 2011, **1**, 425–436; (*c*) R. N. Dhital, C. Kamonsatikul, E. Somsook, K. Bobuatong, M. Ehara, S. Karanjit and H. Sakurai, *J. Am. Chem. Soc.*, 2012, **134**, 20250–20253; (*d*) H. Zhang, T. Watanabe, M. Okumura, M. Haruta and N. Toshima, *Nat. Mater.*, 2012, **11**, 49–52.

17 H. Hirai, S. Takano, T. Nakashima, T. Iwasa, T. Taketsugu and T. Tsukuda, *Angew. Chem., Int. Ed.*, 2022, **61**, e202207290.

18 S. G. Bott, H. Fleischer, M. Leach, D. M. P. Mingos, H. Powell, D. J. Watkin and M. J. Watson, *J. Chem. Soc., Dalton Trans.*, 1991, 2569–2578.

19 S. Takano, H. Hirai, T. Nakashima, T. Iwasa, T. Taketsugu and T. Tsukuda, *J. Am. Chem. Soc.*, 2021, **143**, 10560–10564.

20 J. F. Alvino, T. Bennett, D. Anderson, B. Donoeva, D. Ovoshchnikov, R. H. Adnan, D. Appadoo, V. Golovko, G. Andersson and G. F. Metha, *RSC Adv.*, 2013, **3**, 22140.

21 T. Bennett, A. J. Falcinella, R. J. White, R. H. Adnan, V. Golovko, G. G. Andersson and G. F. Metha, *RSC Adv.*, 2015, **5**, 74499–74505.

22 (*a*) M. J. Hostetler, J. J. Stokes and R. W. Murray, *Langmuir*, 1996, **12**, 3604–3612; (*b*) J. Petroski, M. Chou and C. Creutz, *J. Organomet. Chem.*, 2009, **694**, 1138–1143; (*c*) A. Tlahuice-Flores, *Prog. Nat. Sci.: Mater. Int.*, 2016, **26**, 510–515; (*d*) A. Tlahuice-Flores, *Mol. Simul.*, 2013, **39**, 428–431; (*e*) A. Wing-Bocanegra and A. Tlahuice-Flores, *Phys. Chem. Chem. Phys.*, 2019, **21**, 23855–23864.

23 A. Tlahuice-Flores, R. L. Whetten and M. Jose-Yacaman, *J. Phys. Chem. C*, 2013, **117**, 12191–12198.

24 T. Bennett, R. H. Adnan, J. F. Alvino, V. Golovko, G. G. Andersson and G. F. Metha, *Inorg. Chem.*, 2014, **53**, 4340–4349.

25 Y. Zhao and D. G. Truhlar, *Theor. Chem. Acc.*, 2008, **120**, 215–241.

26 H. Dunning and P. J. Hay, in *Gaussian Basis Sets for Molecular Calculations*, ed. H. F. Schaefer, Springer US, Boston, MA, 1977, pp. 1–27.

27 M. J. Frisch, G. W. Trucks, H. B. Schlegel, G. E. Scuseria, M. A. Robb, J. R. Cheeseman, G. Scalmani, V. Barone, G. A. Petersson, H. Nakatsuji, X. Li, M. Caricato, A. V. Marenich, J. Bloino, B. G. Janesko, R. Gomperts, B. Mennucci, H. P. Hratchian, J. V. Ortiz, A. F. Izmaylov, J. L. Sonnenberg, D. Williams-Young, F. Ding, F. Lipparini, F. Egidi, J. Goings, B. Peng, A. Petrone, T. Henderson, D. Ranasinghe, V. G. Zakrzewski, J. Gao, N. Rega, G. Zheng, W. Liang, M. Hada, M. Ehara, K. Toyota, R. Fukuda, J. Hasegawa, M. Ishida, T. Nakajima, Y. Honda, O. Kitao, H. Nakai, T. Vreven, K. Throssell, J. A. Montgomery Jr., J. E. Peralta, F. Ogliaro, M. J. Bearpark, J. J. Heyd, E. N. Brothers, K. N. Kudin, V. N. Staroverov, T. A. Keith, R. Kobayashi, J. Normand, K. Raghavachari, A. P. Rendell, J. C. Burant, S. S. Iyengar, J. Tomasi, M. Cossi, J. M. Millam, M. Klene, C. Adamo, R. Cammi, J. W. Ochterski, R. L. Martin, K. Morokuma, O. Farkas, J. B. Foresman and D. J. Fox, *Gaussian 16, Revision C.01*, 2016.

28 F. H. Allen, *Acta Crystallogr., Sect. B: Struct. Sci.*, 2002, **58**, 380–388.

29 J. Kilmartin, R. Sarip, R. Grau-Crespo, D. Di Tommaso, G. Hogarth, C. Prestipino and G. Sankar, *ACS Catal.*, 2012, **2**, 957–963.

30 O. D. Haeberlen and N. Roesch, *J. Phys. Chem.*, 1993, **97**, 4970–4973.

31 V. Q. Vuong, J. M. L. Madridejos, B. Aradi, B. G. Sumpter, G. F. Metha and S. Irle, *Chem. Sci.*, 2020, **11**, 13113–13128.

32 A. O. Borissova, A. A. Korlyukov, M. Y. Antipin and K. A. Lyssenko, *J. Phys. Chem. A*, 2008, **112**, 11519–11522.

33 P. Schwerdtfeger, H. L. Hermann and H. Schmidbaur, *Inorg. Chem.*, 2003, **42**, 1334–1342.

34 D. P. Anderson, R. H. Adnan, J. F. Alvino, O. Shipper, B. Donoeva, J.-Y. Ruzicka, H. Al Qahtani, H. H. Harris, B. Cowie, J. B. Aitken, V. B. Golovko, G. F. Metha and G. G. Andersson, *Phys. Chem. Chem. Phys.*, 2013, **15**, 14806.

35 D. P. Anderson, R. H. Adnan, J. F. Alvino, O. Shipper, B. Donoeva, J.-Y. Ruzicka, H. Al Qahtani, H. H. Harris, B. Cowie, J. B. Aitken, V. B. Golovko, G. F. Metha and G. G. Andersson, *Phys. Chem. Chem. Phys.*, 2013, **15**, 14806.

36 T. Omoda, S. Takano and T. Tsukuda, *Small*, 2021, **17**, 2001439.

37 M. Walter, J. Akola, O. Lopez-Acevedo, P. D. Jadzinsky, G. Calero, C. J. Ackerson, R. L. Whetten, H. Grönbeck and H. Häkkinen, *Proc. Natl. Acad. Sci. U. S. A.*, 2008, **105**, 9157–9162.

38 S. Yamazoe, S. Matsuo, S. Muramatsu, S. Takano, K. Nitta and T. Tsukuda, *Inorg. Chem.*, 2017, **56**, 8319–8325.

39 S. G. Bott, D. M. P. Mingos and M. J. Watson, *J. Chem. Soc., Chem. Commun.*, 1989, 1192–1193.

40 (*a*) J. M. L. Madridejos, T. Harada, A. J. Falcinella, T. D. Small, V. B. Golovko, G. G. Andersson, G. F. Metha and T. W. Kee, *J. Phys. Chem. C*, 2021, **125**, 2033–2044; (*b*) S. Muramatsu, Y. Nakahigashi, T. Omoda, S. Takano, T. Tsukuda and Y. Inokuchi, *J. Phys. Chem. Lett.*, 2023, **14**, 5641–5647.

41 L. Lin, P. Claes, P. Gruene, G. Meijer, A. Fielicke, M. T. Nguyen and P. Lievens, *Chem. Phys. Chem.*, 2010, **11**, 1932–1943.

42 (*a*) H. E. Sauceda, D. Mongin, P. Maioli, A. Crut, M. Pellarin, N. Del Fatti, F. Vallée and I. L. Garzón, *J. Phys. Chem. C*, 2012, **116**, 25147–25156; (*b*) B. Lan and D. Y. Sun, *Phys. Rev. B*, 2021, **103**, 1–8.

43 (*a*) J. F. Parker, J.-P. Choi, W. Wang and R. W. Murray, *J. Phys. Chem. C*, 2008, **112**, 13976–13981; (*b*) B. Varnholt, P. Oulevey, S. Luber, C. Kumara, A. Dass and T. Bürgi, *J. Phys. Chem. C*, 2014, **118**, 9604–9611.

44 Q. Martinet, A. Berthelot, A. Girard, B. Donoeva, C. Comby-Zerbino, E. Romeo, F. Bertorelle, M. van der Linden, N. Tarrat, N. Combe and J. Margueritat, *J. Phys. Chem. C*, 2020, **124**, 19324–19332.